JCI insight

RESEARCH ARTICLE

Longitudinal PET imaging demonstrates biphasic CAR T cell responses in survivors

Yogindra Vedvyas,[1,2] Enda Shevlin,[1] Marjan Zaman,[1] Irene M. Min,[3] Alejandro Amor-Coarasa,[1] Spencer Park,[1,2] Susan Park,[1] Keon-Woo Kwon,[1] Turner Smith,[1] Yonghua Luo,[1] Dohyun Kim,[1] Young Kim,[1,4] Benedict Law,[1] Richard Ting,[1] John Babich,[1] and Moonsoo M. Jin[1,2,3]

[1]Molecular Imaging Innovations Institute, Department of Radiology, Weill Cornell Medicine, New York, New York, USA. [2]Department of Biomedical Engineering, Cornell University, Ithaca, New York, USA. [3]Department of Surgery, Weill Cornell Medicine, New York, New York, USA. [4]Department of Pathology, Chonnam National University Medical School, Gwangju, South Korea.

Clinical monitoring of adoptive T cell transfer (ACT) utilizes serial blood analyses to discern T cell activity. While useful, these data are 1-dimensional and lack spatiotemporal information related to treatment efficacy or toxicity. We utilized a human genetic reporter, somatostatin receptor 2 (SSTR2), and PET, to quantitatively and longitudinally visualize whole-body T cell distribution and antitumor dynamics using a clinically approved radiotracer. Initial evaluations determined that SSTR2-expressing T cells were detectable at low densities with high sensitivity and specificity. SSTR2-based PET was applied to ACT of chimeric antigen receptor (CAR) T cells targeting intercellular adhesion molecule-1, which is overexpressed in anaplastic thyroid tumors. Timely CAR T cell infusions resulted in survival of tumor-bearing mice, while later infusions led to uniform death. Real-time PET imaging revealed biphasic T cell expansion and contraction at tumor sites among survivors, with peak tumor burden preceding peak T cell burden by several days. In contrast, nonsurvivors displayed unrelenting increases in tumor and T cell burden, indicating that tumor growth was outpacing T cell killing. Thus, longitudinal PET imaging of SSTR2-positive ACT dynamics enables prognostic, spatiotemporal monitoring with unprecedented clarity and detail to facilitate comprehensive therapy evaluation with potential for clinical translation.

Introduction

Adoptive T cell transfer (ACT) of cytotoxic T lymphocytes is being studied as a potent treatment strategy for cancers that are refractory to standard chemotherapy and radiation therapy. Clinical advances have been made in patients with metastatic melanoma using autologous tumor-infiltrating lymphocytes (TILs) and in several B cell malignancies using autologous chimeric antigen receptor–modified (CAR-modified) T cells (1). Methods used to predict or monitor the activity of infused T cells in patients provide useful but limited data related to treatment efficacy. Current practices involve serum profiling of cytokines associated with T cell activation, direct enumeration of tumor-specific T cell numbers in peripheral circulation, and tumor biopsies (2, 3). Changes in serum cytokine levels, while useful, likely reflect a broader, systemic immune response, illustrating not only the activation of adoptively transferred T cells, but also their effects on neighboring immune cells and dying tumor cells (4). Similarly, while the quantification of adoptively transferred cells in circulation provides useful information regarding their proliferation, researchers and clinicians are blind as to whether the dynamism in T cell numbers relates to expansion at the primary tumor site, metastatic foci, or at off-tumor sites (5). The ability to map the physical distribution and expansion of adoptively transferred T cells throughout the body in a longitudinal manner could therefore significantly improve real-time monitoring of T cell activity against tumors, potential toxicity from off-tumor-site targeting, and contribute to exploring adjuvant therapies to enhance adoptive T cell efficacy against solid cancers (5–7).

The imaging modalities with the highest potential for whole-body visualization of cell trafficking in humans are magnetic resonance imaging (MRI), single-photon emission computed tomography (SPECT), positron emission tomography (PET)/CT, or PET/MRI techniques for detection of labeled cells and coregistration of anatomical information of the body (8–10). PET is particularly amenable to clinical use as it enables noninvasive, highly sensitive, repetitive, and quantitative imaging of positron-emitting, target-

Authorship note: Y. Vedvyas, E. Shevlin, and M. Zaman contributed equally to this work.

Conflict of interest: The authors have declared that no conflict of interest exists.

Submitted: August 30, 2016
Accepted: October 20, 2016
Published: November 17, 2016

Reference information:
JCI Insight. 2016;1(19):e90064.
doi:10.1172/jci.insight.90064.

specific probes. The introduction of microPET for small-animal imaging has similarly made PET amenable to preclinical studies (11). Ongoing activity of ACT against both on- and off-tumor sites can therefore be monitored in vivo by quantitative, radiotracer-based imaging of T cell distribution and expansion upon interaction with target antigen–expressing cells (2, 10, 12). However, previous attempts to systemically monitor ACT in patients have yet to be adopted (13). Passive labeling of T cells with positron-emitting probes ex vivo has been used to monitor the early-stage migration of infused T cells but suffers from potential inaccuracies due to signals from dead or dying cells, probe dilution upon cell division, and a limited ability to track cells over extended periods of time owing to short probe half-life (10). Alternatively, the stable transduction of T cells with a specific reporter gene allows for extended longitudinal studies using serial infusions of reporter-specific probes. Additionally, as only live cells are capable of continually expressing the reporter gene, observed signals are limited to these cells only. Current reporter genes used in preclinical and clinical studies are based on both intracellular enzymes, e.g., herpes simplex virus type-1 thymidine kinase (HSV1-tk) and human deoxycytidine kinase (14–16), and surface receptors, e.g., sodium iodide symporter (NIS) (17), prostate-specific membrane antigen (PSMA) (18), and SSTR2 (19). However, previous imaging studies have failed to demonstrate quantitative monitoring of critical T cell efficacy parameters, namely, whole-body, longitudinal visualization of T cell dynamics spanning initial localization, expansion, and subsequent contraction at primary and/or metastatic tumor sites, and the relationship between these parameters and tumor killing (5, 13, 20–22). More importantly, imaging studies have yet to fully define treatment response parameters or prognostic markers of ACT efficacy and toxicity, and how these affect clinical outcomes in patients.

We have chosen human SSTR2 as a reporter marker in efforts to determine the detection limit of T cells infiltrating solid tumors, and to predict the temporal kinetics of T cell recruitment and expansion, directly related to T cell activity against tumors. SSTR2 belongs to a family of G protein–coupled receptors, with expression restricted to the cerebrum and kidneys, and at low levels in the gastrointestinal tract (23). It is a potentially ideal reporter marker for monitoring ACT owing to its limited basal expression throughout the body and the availability of clinically approved radiotracers for SSTR2, for example, gallium-68–chelated octreotide analogues (^{68}Ga-DOTATOC) for the detection of SSTR2-overexpressing neuroendocrine tumors (19, 24–26). To determine the detection limit of T cells within a solid tumor mass, we introduced SSTR2 into Jurkat T cells and titrated these with wild-type Jurkats to produce subcutaneous Jurkat tumor xenografts, each with defined ratios of SSTR2-expressing cells ranging from 0% to 100%. With this model, it became possible to replicate the varying degrees of T cell localization, penetration, and expansion at or within the tumor site. Over the course of tumor growth, PET/CT imaging was performed using ^{68}Ga-DOTATOC to quantify the detection limit of SSTR2-positive T cells within the tumor and to correlate radiotracer uptake with tumor size and percentages of SSTR2-expressing cells. To further demonstrate the utility of SSTR2 for imaging T cell distribution and expansion in a more physiologically relevant setting, we designed a single lentivirus vector to engineer primary human T cells to express both SSTR2 and a CAR specific to intercellular adhesion molecule-1 (ICAM-1), which is overexpressed in a range of malignant cancers (27–32). Longitudinal, whole-body imaging of SSTR2-expressing, ICAM-1–specific CAR T cells by PET/CT was then performed in mice with systemic growth of poorly differentiated, radioactive iodine–resistant, anaplastic thyroid tumors (33, 34). The kinetics of ^{68}Ga-DOTATOC uptake in survivors demonstrated a biphasic T cell expansion and contraction pattern, the timing of which largely matched tumor burden kinetics except for a consistent lag in T cell contraction after tumor destruction. In contrast, unabated increases in ^{68}Ga-DOTATOC uptake and tumor burden combined with rapid weight loss were observed in nonsurvivors, providing evidence that the rate of tumor killing by T cells in these instances is outpaced by that of tumor growth.

Results

Expression and characterization of SSTR2 in Jurkat T cells. We constructed a lentivirus vector for expression of SSTR2 by inserting the human SSTR2 gene downstream of the elongation factor-1α promoter (35). With increasing lentivirus titer, 100% of Jurkat T cells were transduced to express SSTR2 as measured by antibody binding (Figure 1A). Consistent with agonist-induced internalization of SSTR2 (36), incubation of T cells with the synthetic SSTR2 agonist octreotide reduced surface expression of SSTR2, as indicated by reduced antibody binding (Figure 1B). Labeling of SSTR2-transduced Jurkat T cells with ^{68}Ga-DOTATOC (hereafter referred to as DOTATOC) at concentrations ranging from 8 nM to 250 nM followed a first-order

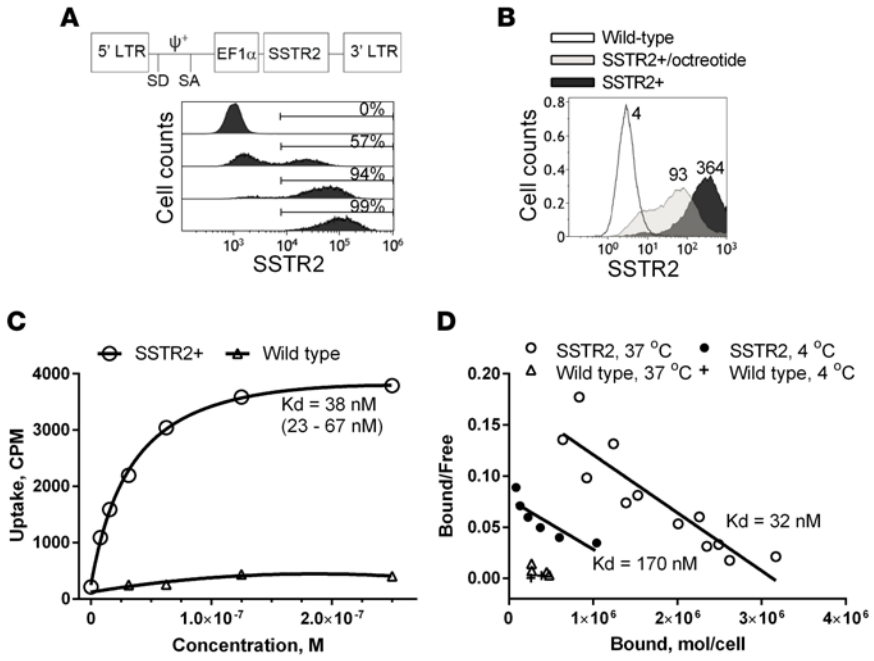

Figure 1. Expression of human SSTR2 by lentivirus vector in T cells. (**A**) A schematic of the lentivirus vector encoding human SSTR2 is shown. LTR, long terminal repeat; SD, splice donor; SA, splice acceptor; EF1α, elongation factor 1α promoter; ψ+, encapsidation signal. Histograms show the level of SSTR2-specific antibody binding to wild-type Jurkat T cells (0%, top) and Jurkat T cells transduced with increasing virus titers. Percentages of SSTR2-positive cells are indicated. (**B**) Level of SSTR2-specific antibody binding to SSTR2-transduced Jurkat T cells with and without preincubation with 1 μM octreotide (37°C, 30 minutes). The numbers denote mean fluorescence intensity. (**C**) DOTATOC uptake by SSTR2-transduced and wild-type Jurkat T cells versus input DOTATOC concentration is shown. A first-order Langmuir isotherm equation was used to fit the data and to find the equilibrium dissociation constant (Kd). Confidence interval of Kd is shown in parentheses. (**D**) DOTATOC uptake at 37°C and 4°C by SSTR2-transduced and wild-type Jurkat T cells is shown via Scatchard plot. Predicted Kd is shown. Data shown are from 3 independent experiments. CPM, counts per minute.

Langmuir isotherm equation, giving a dissociation constant (Kd) of 38 nM (Figure 1C). In comparison, DOTATOC uptake by nontransduced T cells was approximately 10-fold lower. Similar to the Kd estimated by Langmuir isotherm, Scatchard analysis estimated the Kd of DOTATOC to be 32 nM and the site density of SSTR2 to be approximately 3.2×10^6 molecules per cell (Figure 1D). Actual site density is likely to be lower due to recycling of SSTR2 after internalization of DOTATOC and some level of nonspecific binding. Incubation of cells at 4°C to inhibit SSTR2 recycling resulted in an estimated site density of 1.8×10^6 molecules per cell; however, the affinity of DOTATOC for SSTR2 was also determined to be substantially lower (Kd = 170 nM) at this temperature (Figure 1D).

PET imaging of DOTATOC uptake in SSTR2⁺ T cell xenografts. To examine the utility of SSTR2 for the detection of sparsely distributed T cells in tumors, we produced subcutaneous Jurkat T cell xenografts in mice with a mixture of SSTR2-transduced (referred to as SSTR2⁺) and nontransduced (wild-type) cells. These were titrated against each other immediately prior to xenografting to vary the levels of SSTR2-expressing cells within tumors from 0% to approximately 100%. Xenografted Jurkat T cell tumors began to show palpable growth at ~30 days after xenograft and exhibited continuous growth for the next 25 days, reaching approximately 0.7 cm^3 (Figure 2A). Longitudinal measurement of tumor size across different SSTR2⁺ tumors revealed that the level of SSTR2 expression had no significant effect on the growth of Jurkat T cell tumors (Supplemental Figure 1A; supplemental material available online with this article; doi:10.1172/jci.insight.90064DS1). We tested our ability to detect SSTR2⁺ T cells within tumors when both their tumor density and absolute numbers ranged from low to high in both respects. Thus, to cover this range, we initiated PET/CT imaging 12 days after xenograft of 0% to 100% SSTR2⁺ tumors, that is, before we could detect palpable tumor growth, and continued imaging until 56 days after xenograft (Figure 2B). The level of DOTATOC uptake by tumors was quantified as percentage injection dose per volume (%ID/cm^3) based on the region of interest (ROI) enclosing tumors. The ROIs were defined by tumor-size measurements and anatomical information from CT images. Over the course of tumor growth, DOTATOC uptake was higher in tumors comprising increasing percentages of SSTR2⁺ cells (Figure 2B). PET/CT images showed DOTATOC uptake by tumors and uniformly higher uptake by the kidneys and bladder — consistent with its known biodistribution and renal clearance (Figure 2C) (19). DOTATOC uptake values, as measured by %ID/cm^3, agreed with visual assessments of PET/CT images over the course of tumor growth and correlated with increasing SSTR2⁺ percentages within the tumors (Figure 2, B and C, and Supplemental Figure 2). We also noted a minor increase in DOTATOC uptake during growth of 0% SSTR2⁺ tumors, which we speculate to be caused by the increasing leaky vasculature and stagnant blood pooling within tumors (Figure 2B).

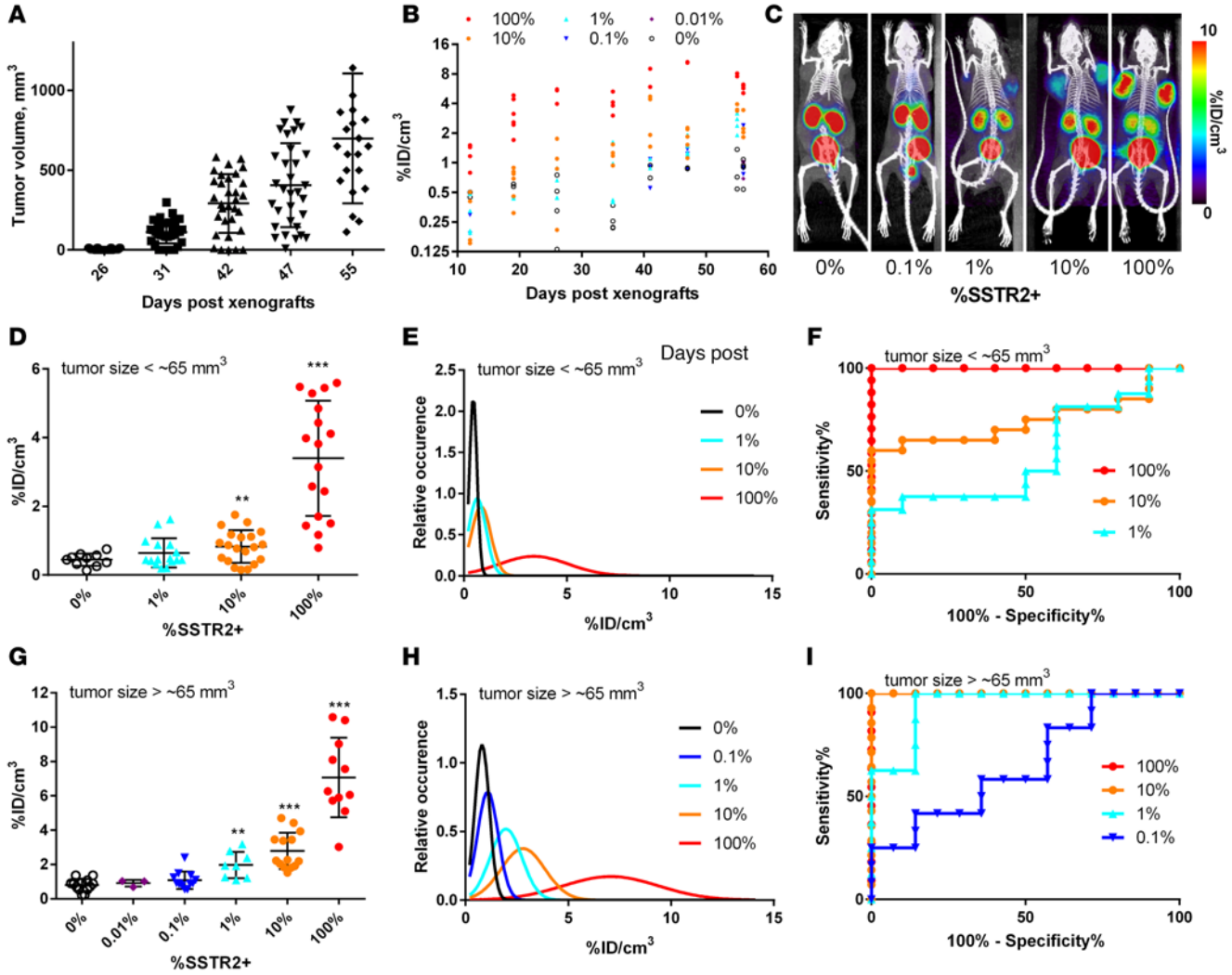

Figure 2. Quantitative PET/CT measurement of DOTATOC uptake by Jurkat tumors and statistical analysis. (**A**) Tumor volume (mm^3) plotted against number of days after xenograft. (**B**) Measured DOTATOC uptake is quantified as percentage injection dose per volume (%ID/cm^3) for Jurkat tumors (100%–0% $SSTR2^+$) over the course of tumor growth. (**C**) Representative PET/CT images of mice xenografted with Jurkat T cells at 0%, 0.1%, 1%, 10%, and 100% SSTR2 expression. Images are maximum intensity projections (MIPs) of the entire mouse body (~20-mm-thick plane). PET intensity is pseudocolored in the range of 0–10 %ID/cm^3. (**D** and **G**) DOTATOC uptake (%ID/cm^3) for Jurkat tumors less or greater than 65 mm^3, respectively. (**E** and **H**) Simulated Gaussian distribution as a function of the measured mean and standard deviation of DOTATOC uptake for each percentage $SSTR2^+$ tumor when the volume is less or greater than 65 mm^3, respectively. (**F** and **I**) Receiver operating characteristic (ROC) curves of percentage sensitivity and specificity are shown for tumors less than 65 mm^3 (**D**) and greater than 65 mm^3 (**G**). ** $P < 0.01$ vs. 0%, *** $P < 0.001$ vs. 0%, by Student's *t* test.

Defining detection limit, specificity, and sensitivity of $SSTR2^+$ T cells. We next analyzed DOTATOC uptake values to determine the detection sensitivity and specificity of SSTR2-expressing T cell density within tumors. Regarding small, palpable tumors (below ~65 mm^3), DOTATOC uptake was slightly higher in those containing 1% $SSTR2^+$ cells (0.64 ± 0.4 %ID/cm^3; $P = 0.1$ vs. 0% $SSTR2^+$), but was significantly higher in tumors containing $SSTR2^+$ T cell densities of 10% (0.83 ± 0.5 %ID/cm^3) and 100% (3.4 ± 1.7 %ID/cm^3), compared with uptake within 0% $SSTR2^+$ tumors (0.44 ± 0.2 %ID/cm^3) (Figure 2D). Assuming a normal distribution of DOTATOC uptake values (Figure 2E), a threshold of 0.6 %ID/cm^3 was the DOTATOC uptake cutoff in order to obtain 95% specificity (5% false positive rate) for tumors of this size. The detection sensitivity (% true positive rates) for 1%, 10%, and 100% $SSTR2^+$ tumors with the 0.6 %ID/cm^3 threshold was calculated to be 54%, 69%, and 95%, respectively. The detection limit for 10% $SSTR2^+$ tumors below ~65 mm^3 was considered marginally acceptable with an area under the receiver operating characteristic (ROC) curve (AUC) (37) value of 0.75 (Figure 2F). In contrast, DOTATOC uptake for more discernible $SSTR2^+$ tumors (larger than 65 mm^3) was significantly higher within 100%, 10%, and 1% $SSTR2^+$ tumors (7.1 ± 2.3, 2.8 ± 1.1, and 2.0 ± 0.77 %ID/cm^3, respectively) when compared with

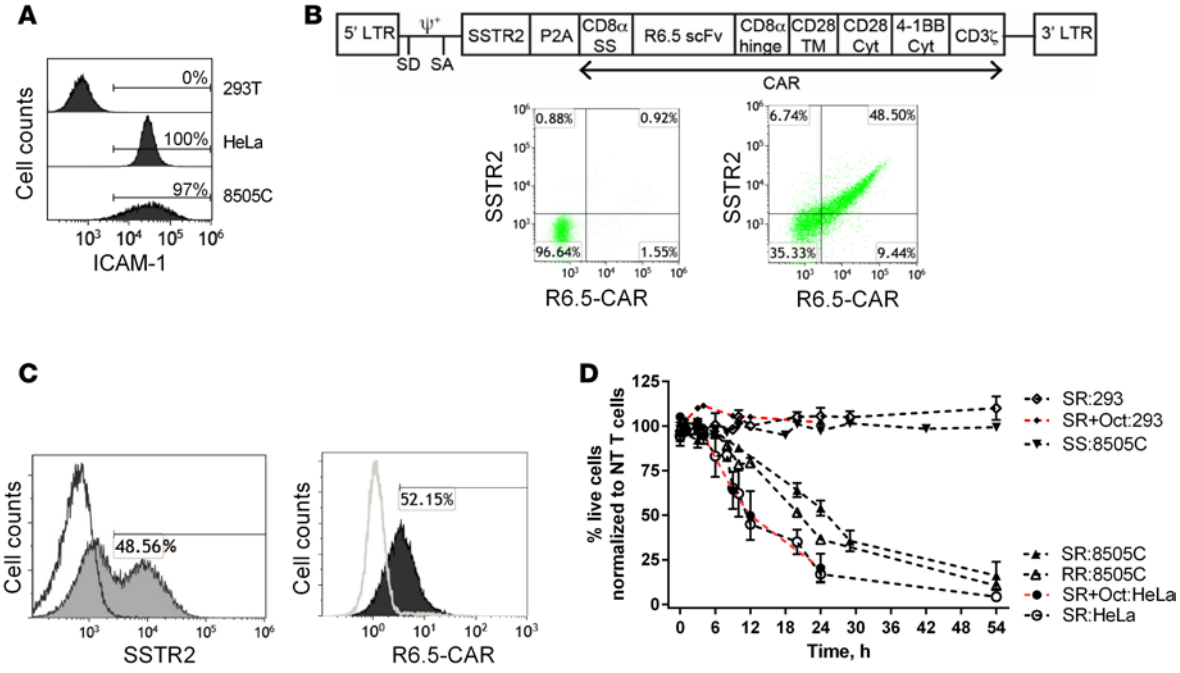

Figure 3. CAR T cell efficacy against thyroid tumor cells in vitro and in vivo. (**A**) Representative histograms showing the level of anti–ICAM-1 antibody binding to ICAM-1–negative HEK 293T, ICAM-1–positive HeLa, and 8505C cells. (**B**) Schematic of the lentivirus vector encoding SSTR2-R6.5-CAR. CD8α SS (signal sequence); TM, transmembrane; Cyt, cytoplasmic domain. Representative dot plots showing anti-SSTR2 and anti-CAR antibody binding to nontransduced (left) and SSTR2-P2A-R6.5-CAR–transduced (right) primary human T cells. (**C**) Primary human T cells were transduced separately with individual vectors encoding either SSTR2 or R6.5-CAR. Representative histograms show anti-SSTR2 antibody binding to either R6.5-CAR– or SSTR2-transduced (filled) and nontransduced (open) primary T cells. (**D**) Effector/target (E:T) assay measuring lysis of target expressing (HeLa and 8505C) or control (HEK 293) cells by CAR T cells at a 2.5:1 E:T ratio. Percentages of live cells were measured by bioluminescence intensity normalized to the levels of target cells incubated with nontransduced T cells. Octreotide (1 μM) was added to SR T cells as indicated (SR+Oct). n = 3–6 from 3 different donor T cells. NT, nontransduced T cells; SS, SSTR2-transduced T cells; RR, R6.5-CAR–transduced T cells; SR, SSTR2-R6.5-CAR–transduced T cells.

background uptake by 0% SSTR2$^+$ tumors (0.8 ± 0.35 %ID/cm^3) (Figure 2G). Uptake was also detectable, although not significant, even within 0.1% SSTR2$^+$ tumors (1.1 ± 0.51 %ID/cm^3, P = 0.12). A DOTATOC uptake cutoff of 1.1 %ID/cm^3 gave 95% specificity and 87% sensitivity for 1% SSTR2$^+$ tumors within the Jurkat model (Figure 2H). With the same threshold, one achieves greater than 95% sensitivity for tumors in which the SSTR2$^+$ T cell density is at or above 10%. The ROC curve of DOTATOC uptake by 1% SSTR2$^+$ tumors gives 0.95 AUC, while 0.1% SSTR2$^+$ tumors gives 0.68 AUC (Figure 2I). SSTR2$^+$ T cells in culture were ~100% SSTR2$^+$ by antibody staining (Supplemental Figure 1B). However, later resection of 100% SSTR2$^+$ tumors followed by staining for SSTR2 by flow cytometry revealed that the level of SSTR2 expression was reduced to ~80%, with the 20% reduction reflecting the presence of mouse stromal cells within tumors (Supplemental Figure 1, B and C). The reduction of SSTR2 expression was not caused by the loss of SSTR2 expression during tumor growth, as a similar level of reduction was seen by CD3 staining: 70% CD3$^+$ in cells harvested from tumors, reduced from 80%–85% CD3$^+$ from the same cells in culture.

To express the observed SSTR2$^+$ T cell tumor density as an absolute number per volume, we resected Jurkat tumors and determined the average total cell density to be 5.1 ± 1.3 × 10^8/cm^3 (n = 4). Accordingly, 1% SSTR2$^+$ tumors (comprising approximately 4 × 10^8/cm^3 Jurkat T cells and 1 × 10^8/cm^3 stroma) would contain ~4 × 10^6 SSTR2$^+$ T cells per cm^3. Based on the data obtained using the Jurkat model, we proceeded to utilize SSTR2-based PET imaging to estimate and longitudinally monitor the density of reporter-expressing CAR T cells infiltrating solid tumors.

Efficacy of ICAM-1–specific CAR T cells against thyroid tumor cells. Radioiodine-resistant, poorly differentiated thyroid cancers have been found to overexpress ICAM-1 at levels correlating with tumor malignancy and metastatic potential (30). The anaplastic thyroid cancer cell line 8505C was also found to be ICAM-1 positive (Figure 3A), the level of which varied due to culture conditions and growth in vivo. The anti–ICAM-1 CAR is third generation and consists of an ICAM-1–specific single-chain variable fragment (scFv) from the R6.5

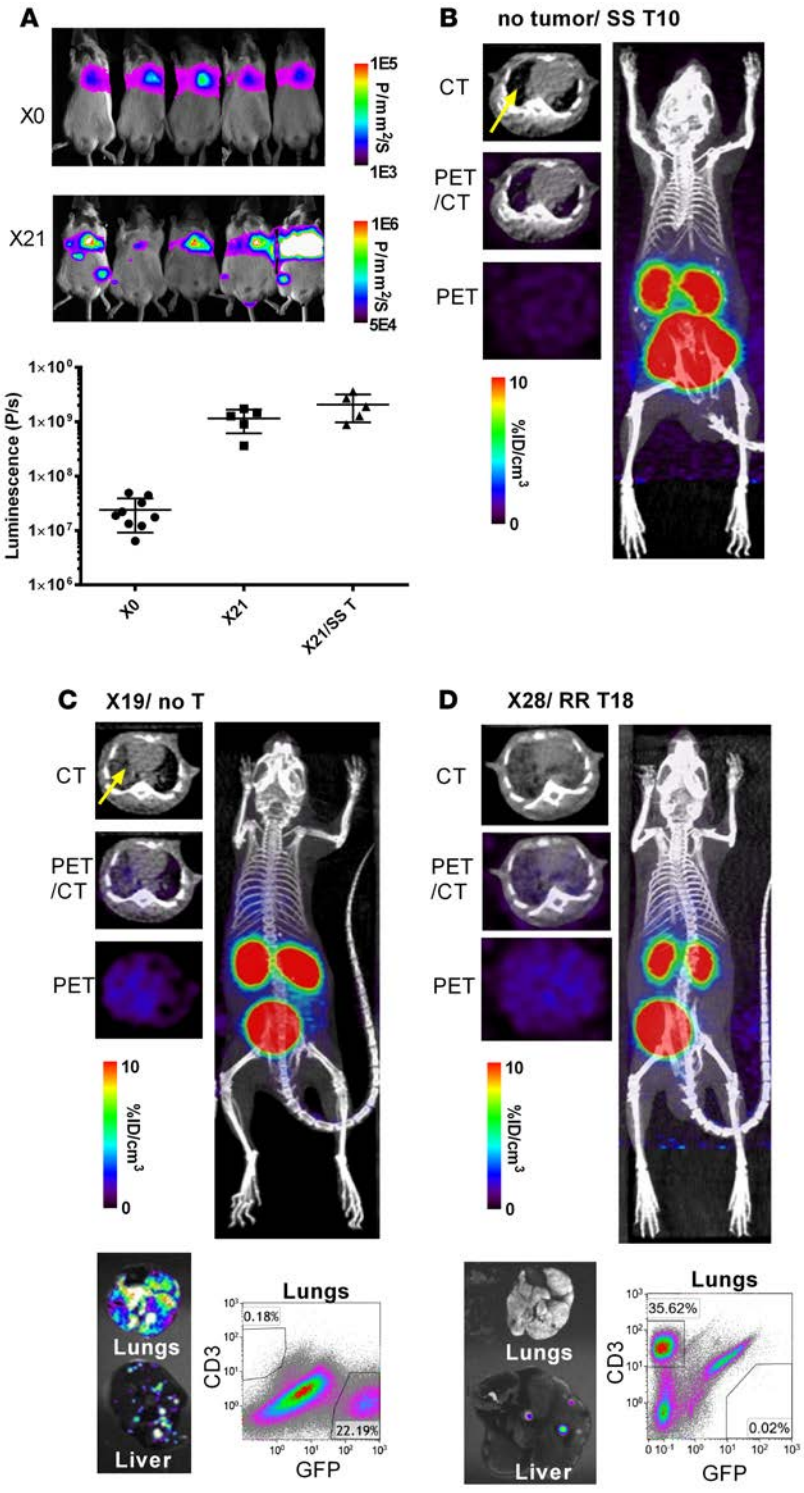

Figure 4. Whole-body imaging of tumor growth by luminescence and DOTATOC uptake by PET/CT. (**A**) Tumor burden from day of intravenous tumor xenograft via tail vein (X0) and 21 days after (X21) was visualized and quantified by bioluminescence. (**B**–**D**) Transverse CT-only, PET-only, and PET/CT superimposed images are shown alongside a coronal view of the entire mouse body. PET images are drawn in indicated ranges. Ex vivo fluorescence images of lungs and liver are shown together with flow cytometry analysis of the $CD3^+$ (T cell) and GFP^+ (tumor cell) populations of the same lungs are also shown (**C** and **D**). Each PET/CT image is representative of at least 3 independent experiments. SS, SSTR2-transduced T cells; RR, R6.5-CAR–transduced T cells; no T, no T cell treatment.

antibody (38), the transmembrane and cytoplasmic domains of CD28, followed by CD137 and CD3ζ (35). A lentiviral vector encoding both SSTR2 and R6.5-CAR was constructed by linking SSTR2 to the R6.5-CAR with a ribosome-skipping porcine teschovirus-1 2A (P2A) sequence (39) (Figure 3B). Primary T cells were transduced to express SSTR2 and R6.5-CAR at approximately 50% (Figure 3B). Expression levels of both SSTR2 and R6.5-CAR obtained via the single SSTR2-R6.5-CAR (SR) vector were comparable to what could be attained by separate SSTR2 (SS) and R6.5-CAR (RR) vectors at similar virus titers (Figure 3, B and C). To test the selectivity of CAR T cell–mediated killing of 8505C cells, we also used the cervical cancer cell line, HeLa, exhibiting high basal levels of ICAM-1, and the ICAM-1–negative cell line, HEK 293, as positive and negative controls, respectively (Figure 3A). All target cells were lentivirally transduced to express GFP and firefly luciferase in order to quantitatively monitor cell viability. Incubation of CAR T cells with ICAM-1–positive and –negative cell lines showed that CAR T cell killing of target was strictly dependent upon ICAM-1 expression. After 24 hours, 17% ± 11% of HeLa and 52% ± 15% of 8505C cells were viable at effector to target (E:T) ratios of 2.5:1, with no killing of HEK 293 cells observed (106% ± 8%) (Figure 3D). Additionally, no killing of 8505C cells (97% ± 2%) was observed upon coincubation with SS T cells. The rate of killing of 8505C cells by RR and SR T cells, and that of HeLa by SR T cells with or without the addition of octreotide (1 μM) was comparable. This confirmed that SSTR2 expression on T cells, as well as binding of its cognate ligand (DOTATOC), does not alter CAR T cell functionality.

Longitudinal PET imaging of $SSTR2^+$ CAR T cells in vivo. In order to test the ability of an SSTR2-based reporter system to acquire in vivo visual mapping of CAR T cell localization and antitumor dynamics, NSG mice were first xenografted by systemic injection of 1×10^6 8505C-$FLuc^+GFP^+$ cells. Bioluminescence imaging demonstrated that primary 8505C tumors localized to the lungs, with metastases occurring within the liver and at more distant sites (Figure 4A), consistent with previously reported observations of 8505C

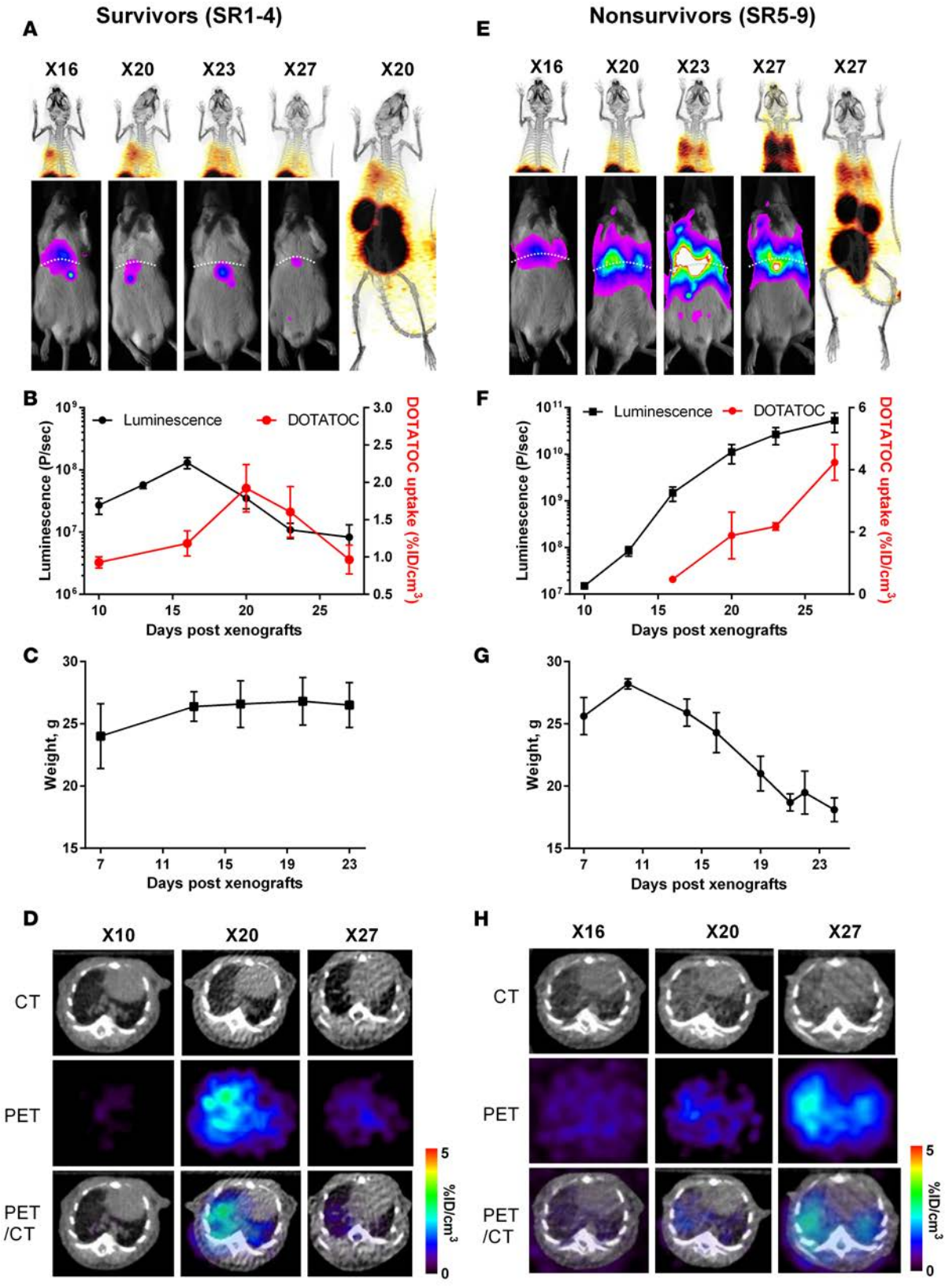

Figure 5. Quantitative PET for detection of CAR T cells and luminescence of tumor burden in survivors vs. nonsurvivors. Representative longitudinal, PET/CT (coronal view of 20-mm-thick plane, maximum intensity projection [MIP]) and concurrent bioluminescence imaging of survivors (n = 4) (**A**) vs. nonsurvivors (n = 5) (**E**). Diaphragms are traced with dotted lines, drawn to visualize tumor burdens separately in lungs and liver. Trend-line graphs plot region of interest (ROI) values for DOTATOC uptake (percentage injection dose per volume [%ID/cm^3]) against bioluminescence values (photons [P]/sec) in the lungs taken from the same mice on the same day. Luminescence images are drawn with the same upper bound (10^6 P/mm^2/sec) with gradually

increasing lower bounds (X16, X20 for 2.5×10^4 P/mm^2/sec and X23, X27 for 5×10^4 P/mm^2/sec) for clarity of delineating tumor burden. Longitudinal PET/CT images of the upper body cropped at the kidney apex are drawn with a uniform range of DOTATOC concentrations (0.5–5.0 %ID/cm^3), while whole-body PET/CT images are drawn in 0.5–5.0 %ID/cm^3 for (**A**) and 1–10 %ID/cm^3 for (**E**). Quantification of luminescence and DOTATOC uptake by the lungs (**B** and **F**) and body weight change (**C** and **G**) is shown for survivors and nonsurvivors. Representative longitudinal, PET/CT (transverse view of 1-mm-thick plane, MIP) views of lungs are shown for survivors (**D**) and nonsurvivors (**H**). PET images are drawn in indicated ranges. X, number of days after tumor xenograft; SR, treated with SSTR2-R6.5-CAR–transduced T cells.

tumor growth characteristics in mice (40). Using bioluminescence as a measure of tumor burden, it was observed that an initial infusion of 1×10^6 tumor cells expanded 50- to 100-fold over 21 days (Figure 4A). Tumor growth was not hampered by treatment with SS T cells 10–13 days after tumor xenograft (SS1–5, as defined in Supplemental Figure 3), confirming the absence of nonspecific killing by non-CAR T cells in vivo. Prior to conducting DOTATOC imaging of SR T cells, we first examined the circumstances that give rise to nonspecific DOTATOC uptake, which may include leaky tumor vessels within areas of high tumor burden causing blood pooling. First, CT images of mice with no tumors that were infused with SS T cells showed the heart and tumor-free alveolar air space in the lungs (Figure 4B). The level of DOTATOC uptake in these mice (0.7 %ID/cm^3) was comparable to those in Jurkat tumors containing 0% SSTR2$^+$ cells (0.6–0.8 %ID/cm^3) and is thus indicative of the absence of CAR T cell expansion. In comparison, mice xenografted with 8505C tumors had alveolar air space replaced by the growth of tumor cells (accounting for as much as 22% of total live cells in lungs), which generated increased alveolar tissue density in transverse CT images of these mice (Figure 4C). We observed low yet gradually increasing nonspecific DOTATOC uptake in the thoracic cavity of mice with high tumor burden (1.3 ± 0.5 %ID/cm^3 for 23 to 27 days after tumor xenograft) that received either no T cells or SS T cells. This was found to be due to subjects' poor health and slower heartbeat, causing a longer circulation time and a delay in DOTATOC clearance. Mice treated with RR T cells (RR1–3, Supplemental Figure 3) were also found to show only background levels of DOTATOC uptake in the lungs (1.0 %ID/cm^3) (Figure 4D). This was despite the fact that over the course of tumor killing, RR T cells had expanded such that they accounted for 36% of total live cells in lungs.

After confirming the relative absence of lung-specific DOTATOC uptake related to tumor burden itself or SSTR2-negative T cell expansion, we then treated tumor-bearing mice with SR T cells at days 7, 10, 13, and 15 after xenograft. Mice were subjected to longitudinal bioluminescence and concurrent PET/CT imaging to visualize the relationship between tumor burden and the dynamism of infused SR T cells over the course of their localization, tumor engagement, and killing (Supplemental Figure 3, Supplemental Videos 1 and 2, and Figure 5, A and E). Progressive delays in T cell infusion after tumor xenograft were used in order to observe potential differences in CAR T cell dynamics related to differences in tumor burden. Primary tumor burden in the lungs from mice treated with SR T cells 7 and 10 days after xenograft (SR1–4) began noticeably decreasing at approximately 16 days after tumor xenograft with little change in body weight (Figure 5, A–C). Increasing tumor burden over time correlated with increasing DOTATOC uptake within the lungs, indicating that infused SR T cells had stably localized to the tumor site where they were actively proliferating in response to engagement with ICAM-1–positive tumor cells (Figure 5A). It was also found that peak DOTATOC uptake, and therefore peak CAR T cell expansion, lagged behind peak tumor bioluminescence by approximately 4 days. Peak DOTATOC uptake within the lungs was followed by gradual curtailment and contraction corresponding to diminishing T cell numbers, thus demonstrating a biphasic antitumor CAR T cell response, incorporating classical antigen-mediated T cell expansion followed by T cell contraction upon antigen withdrawal (Supplemental Video 1 and Figure 5A). In contrast with the swift tumor elimination, followed by CAR T cell contraction within the lungs of surviving mice, further delay of treatment with SR T cells to 13 to 15 days after tumor xenograft (SR5–9) failed to reduce tumor burden and restore health before euthanasia was invoked (deemed necessary after a 25%–30% loss in body weight) (Figure 5, E–G). This was despite increasing lung-specific DOTATOC uptake confirming SR T cell expansion in the lungs of these mice (Supplemental Video 2 and Figure 5E). Longitudinal transverse CT images revealed that while tissue density in lungs associated with tumor and CAR T cell burden persisted in nonsurvivors, it was eventually eliminated and reverted to clear, normal alveolar density upon tumor elimination and contraction of T cells in surviving mice (Figure 5, D and H).

Confirmation of PET and bioluminescence imaging by ex vivo analysis. Assessment of CAR T cell–mediated tumor killing by ex vivo fluorescence imaging of the lungs and liver (performed on day 28 after tumor xenograft) confirmed that tumor elimination had indeed occurred in survivors treated with SR T cells on

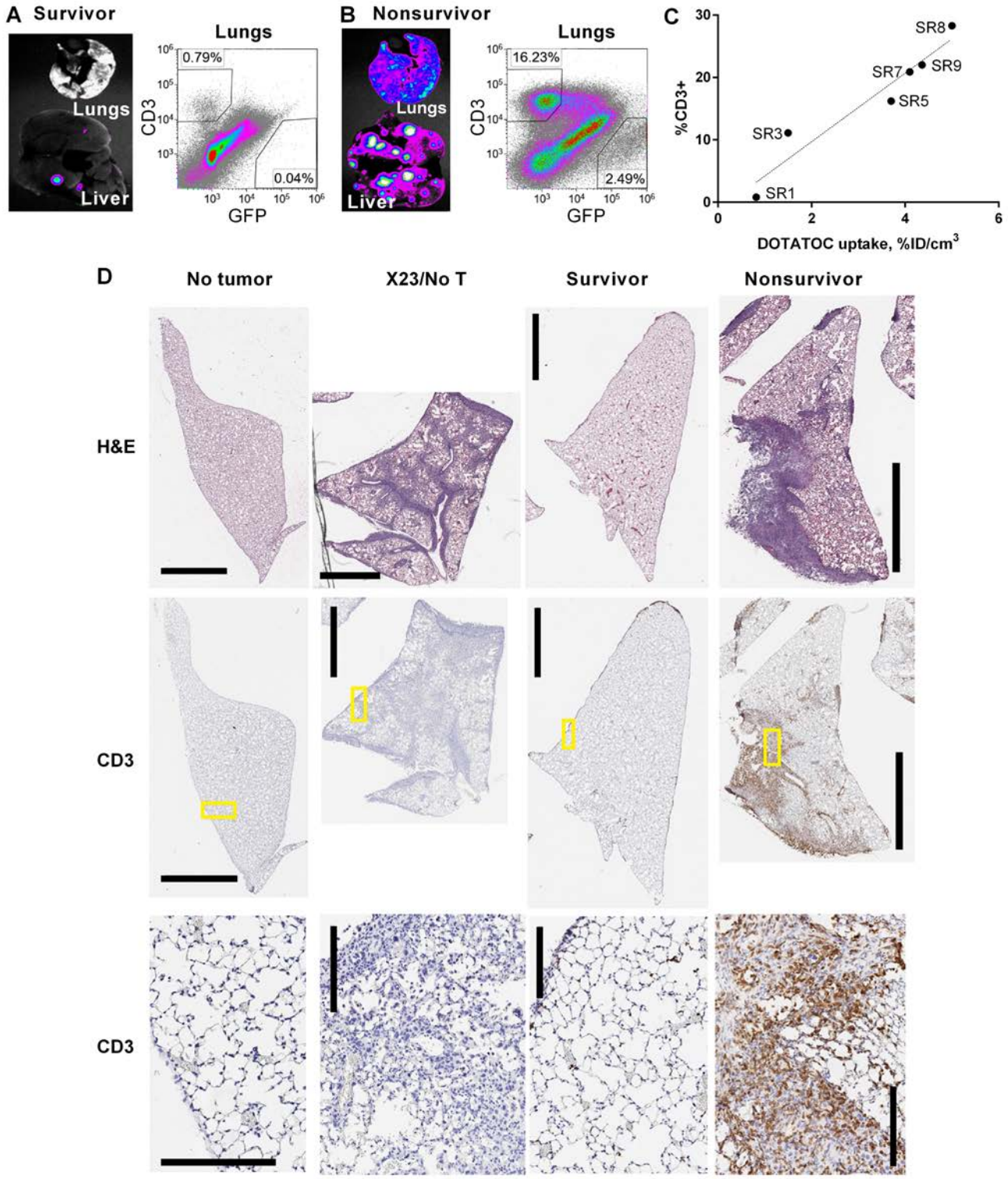

Figure 6. Ex vivo analysis of CAR T cell and tumor density in lungs. Ex vivo, GFP$^+$ tumor cell fluorescence of representative lungs and liver, and flow cytometry of total, live-gated lung cells from (**A**) survivors (n = 4) and (**B**) nonsurvivors (n = 5). Organs were harvested, imaged, and analyzed by flow cytometry on day 28 after xenograft (X28). (**C**) DOTATOC uptake (percentage injection dose per volume [%ID/cm^3]) by the lungs in SR1–SR9 mice are plotted against the percentages of T cells (CD3$^+$) determined by flow cytometry. (**D**) Representative histological images are shown for paraffin-embedded H&E-stained sections of 1 entire lung lobe (top), and anti–human CD3 antibody with hematoxylin counterstain (middle). High-magnification views (yellow boxed regions in middle sections) show tumor cells and CD3-stained T cells (bottom). Tumor cells are identified by dark hematoxylin-stained nuclei. Human CD3$^+$ cells are stained brown. Scale bars: 2 mm (top and middle sections) and 200 μm (bottom sections). Lungs were harvested from healthy mice with no tumor, mice 23 days after tumor xenograft and no T cell treatment (X23/no T cell), and X28 for T cell–treated survivors and nonsurvivors.

days 7–10 after tumor xenograft (Figure 6A). Flow cytometry analysis of lungs that were determined to have undergone CAR T cell contraction by DOTATOC uptake showed that $CD3^+$ cell levels were reduced to less than 1% of total lung cells (Figure 6A). It also confirmed continuing expansion of SR T cells and substantial reduction of tumor burden in nonsurviving mice treated on days 13–15 after tumor xenograft (2.5%), compared with mice that received no T cells (22%) (Figure 6B vs. Figure 4C). Furthermore, plotting the percentage of human $CD3^+$ cells in the lungs of SR-treated mice against DOTATOC uptake from same, demonstrated that CD3 staining by flow cytometry was largely proportional to DOTATOC signal obtained by PET (Figure 6C). The observation that DOTATOC uptake values greater than 3 corresponded to greater than 10% $CD3^+$ T cells was in quantitative agreement with the findings from the Jurkat tumor model (Figure 2, G and H).

Histological analysis of lung tissues further corroborated the conclusions drawn from whole-body PET/bioluminescence imaging, flow cytometry, and ex vivo organ images. Lung tissues from untreated mice (X23/no T cells) revealed extensive infiltration and growth of tumor cells into the alveoli, bronchioles, pulmonary vessels, and pleural spaces compared with their healthy no-tumor counterparts (Figure 6D and Supplemental Figure 4). Lung tissues harvested from survivors (SR1–4) were mostly devoid of tumor infiltrates and SR T cells, and appeared to have restored normal alveoli structure. Nonsurvivor lung tissues (SR5–9) revealed much higher burden of tumor, yet infiltrating T cells (CD3 staining) were found to colocalize with tumor lesions, confirming ongoing tumor elimination by CAR T cells (Figure 6D).

In contrast with the more evenly distributed and synchronized growth of tumors in the lungs, metastatic lesions in the liver were distinctive, isolated, and smaller, measuring only millimeters in size (Figure 4, C and D, Figure 6, A and B, and Supplemental Figure 5). In most cases, these liver metastases would be of insufficient size to generate CAR T cell expansion to requisite densities for visual detection by DOTATOC/PET — even during efficient CAR T cell responses. However, we were able to detect elevated DOTATOC levels in certain livers with tumor metastases as visualized by luminescence, particularly within nonsurvivors (Figure 6B and Supplemental Figure 5B). Such elevated DOTATOC accumulation was scarce in survivors where large tumor lesions in the liver were absent (Figure 6A and Supplemental Figure 5A). Infiltration of CAR T cells into metastatic liver lesions irrespective of their size was also confirmed by histology (Supplemental Figure 5). These data therefore confirmed that dynamic DOTATOC uptake by SSTR2-expressing, adoptively transferred T cells can be used to monitor the presence of T cell infiltrates at both primary tumor sites and metastatic lesions.

Discussion

Recent clinical studies have strived to find both primary and secondary indicators to enable real-time monitoring of adoptively transferred T cell activity and to predict the likelihood of systemic toxicity (41). However, as ACT has demonstrated both profound potency and at times, lethal toxicity, there is a clear need for tracking modalities that can provide additional spatiotemporal information to enable both baseline mapping of T cell localization and real-time visualization of multiple sites of T cell expansion. Quantitative PET imaging is increasingly used for diagnostic purposes and to gauge therapy response in a more accurate and objective manner (42). To our knowledge, this study is the first to utilize PET/CT to conduct high-quality, longitudinal whole-body mapping of ACT localization that illustrates how its dynamics affect the course of treatment and survival outcomes. Furthermore, this was achieved using clinically approved imaging tools to demonstrate critical events such as T cell migration, expansion, peak expansion, and contraction — correlated to tumor burden.

SSTR2 was chosen as a genetic reporter for several reasons. One was to take advantage of the FDA-approved PET radiotracer specific to SSTR2, which is currently in use in clinics to probe for overexpressed SSTR2 in neuroendocrine tumors (43). SPECT-based imaging is also available using ^{111}In-DTPAOC (octreoscan) (44). SSTR2 displays restricted basal expression in tissues and all major organs except in the kidneys and cerebrum, making it ideal for detection of adoptively transferred T cells targeting a multitude of solid tumors. SSTR2 can potentially function as a dual reporter-suicide gene by conjugation of the therapeutic high-energy radioisotopes ^{177}lutetium, ^{90}yttrium, or ^{213}bismuth to DOTATOC instead of ^{68}gallium (25, 45), thus enabling elimination of SSTR2-expressing T cells in the case of CAR T cell toxicity. Compared with HSV1-tk, SSTR2 is surface expressed and therefore does not require prior radioligand internalization into the cell. It has previously been shown that SSTR2 facilitates rapid radiotracer uptake, and this combined with swift renal clearance of unbound DOTATOC means that high-quality, clinical-

grade images can be obtained 1 hour after DOTATOC injection (46) compared with 2 to 3 hours using HSV1-tk–based systems (13, 47). DOTATOC also has a short half-life of 68 minutes which, combined with its rapid clearance, delivers a low radiation dose to the patient. The fact that SSTR2 is of human origin should also limit its immunogenicity, which has plagued experiments using nonhuman genetic reporters (48, 49). Another surface-expressed reporter gene, PSMA, is reportedly superior to more widely tested receptors such as HSV1-tk and NIS for imaging purposes (18). Therefore, with the myriad of available genetic reporters, choosing the most suitable for imaging adoptively transferred T cells will depend foremost on the tumor being targeted. For example, SSTR2 would be unsuitable for imaging ACT targeting neuroendocrine tumors because of its inherent overexpression in this malignancy. Therefore, it is inevitable that were the adoption of human reporter genes to become widespread, a repertoire of multiple reporters would be required to circumvent potential on-target, off–T cell radiotracer uptake. Interestingly, the synchronous use of distinct genetic reporters may create novel opportunities for near-simultaneous live imaging of multiple infused cell populations (50). For example, central memory and naive T cells were recently reported to provide superior antitumor efficacy compared with effector memory cells or clinical products derived from unenriched T cells (51, 52). However, these studies lack in vivo mechanistic data demonstrating the differences in T cell dynamics behind the observations. Coexpression of CAR or T cell receptor with separate population-specific reporter genes, for example SSTR2 and PSMA, followed by sequential, time-delayed injection of cognate PET radiotracers, could reveal underexplored dynamics of, and interactions between, these populations in both clinical and preclinical studies.

Adoptively transferred T cells have been shown to penetrate and distribute throughout tumor tissue (12). The utility of any imaging modality capable of monitoring ACT will therefore depend upon a limit-of-detection threshold sensitive enough to enable monitoring of meaningful T cell activity at low tissue densities. Moreover, evaluation of this detection limit in a physiologically relevant model must also account for the sensitivity and specificity of the infused imaging agent for the reporter in question, whose density at the tumor site will vary exponentially as its cognate T cells expand and contract in response to target elimination. Therefore, to approximate the DOTATOC-based detection limit of tumor-infiltrating SSTR2-transduced T cells, we utilized mosaic tumor xenografts of Jurkat T cells with increasing ratios of SSTR2 expression to create a standard by which quantitative PET signals can be related to T cells of known density within tumors. Using the lentivirus developed in this study, the surface expression of SSTR2 in transduced Jurkat T cells was in the range of several million per cell, a level significantly higher than previously published (19) and therefore likely to extend the lower limit of $SSTR2^+$ T cell detection. We observed that with a known threshold of radiotracer uptake, one can detect tumor-infiltrating T cells down to a minimum density of 0.8% or ~4×10^6 cells/cm^3, with 95% specificity and 87% sensitivity. This compares favorably with a previous report using PET to detect tumor-infiltrating T cells that used flow cytometry–based detection in a separate, equally treated cohort of mice as a reference to purport a tumor-infiltrating T cell detection limit of 0.5% within tumors (53).

To demonstrate the feasibility of SSTR2 reporter–based imaging to predict and monitor tumor-directed T cell activity, we chose ICAM-1–positive anaplastic thyroid cancer cells as a target model and engineered T cells to express both ICAM-1–specific CAR and SSTR2 using a single lentiviral vector. A potential drawback to the use of genetic reporters for imaging receptor-modified ACT is that the T cells in question require the stable expression of 2 separate genes, which can substantially reduce the percentage of cells coexpressing both genes. However, with the use of a self-cleaving P2A sequence (39), we demonstrated that both CAR and reporter genes can be successfully expressed on the same individual cell without compromising the level of expression otherwise achievable using 2 independent vectors.

T cells expressing the SSTR2-R6.5 CAR efficiently and specifically lysed ICAM-1–expressing 8505C and HeLa tumor cell lines within 24 hours, as monitored by bioluminescence, while leaving ICAM-1–negative HEK293 cells largely untouched. Furthermore, efficient killing was also observed at lower E:T ratios, thus demonstrating both specificity and high activity of the SSTR2-R6.5 CAR for ICAM-1–expressing target cells. This targeting efficacy was replicated in vivo, as treatment of 8505C tumor-bearing mice with SSTR2-R6.5-CAR T cells resulted in a significant reduction in tumor burden across all treated mice compared with those that received T cells expressing SSTR2 only. Tumor lysis occurred 1–2 weeks after treatment, with the time required for CAR T cell–mediated tumor reduction correlating with tumor burden at time of treatment. Expanding SSTR2-R6.5-CAR T cells at the tumor site were visualized via increasing DOTATOC signals. PET imaging of SSTR2-R6.5-CAR T cells was sensitive enough to visualize

their perfusion throughout the lungs such that the lung footprint and outline became distinguishable by the presence of T cells alone. This was confirmed by histological analysis of tissue sections, which demonstrated the ubiquitous presence of human $CD3^+$ T cells throughout the lungs of treated mice. Despite the small size (several mm) of metastatic nodules in the liver, localized DOTATOC accumulation was also recorded, which coincided with the emergence, followed by attenuation, of distinct liver tumor nodules as detected by bioluminescence imaging. Extrapolation of the image quality and sensitivity obtained in the current study to similar scenarios in humans would likely enable equal if not better monitoring of ACT tracking to primary, metastatic, and critically, to on-target, off-tumor sites. Visualization of ACT expansion may even draw attention to previously undetected metastatic sites such that sufficiently sensitive reporter imaging of ACT may provide additional theranostic capabilities.

Because of reported dose-limiting toxicity, the number of modified T cells infused to patients is typically in the range of 1×10^6 to 10×10^6 T cells/kg (2, 3, 41, 54), and target-mediated expansion and persistence of T cells is therefore a prerequisite for substantive tumor destruction to occur. Indeed, it has been reported that higher peak expansion of infused T cells correlates with increased rates of disease remission (2, 54). Tumor-bearing mice in the current study were treated with approximately 1.5×10^6 SSTR2-CAR^+ T cells at days 7–15 after xenograft. Subsequent longitudinal monitoring of both tumor growth and CAR T cell expansion at the tumor site enabled several observations to be made. Timely infusion of CAR T cells resulted in survival of all subjects without weight loss, while later treatments led to uniform death despite evidence of tumor killing by CAR T cells. Survivors exhibited a biphasic pattern of DOTATOC uptake within the lungs, with a similar luminescence pattern observed regarding primary lung tumors. A notable feature of this correlative pattern was that the peak DOTATOC signal, and therefore peak T cell expansion, lagged behind peak tumor burden by several days. This expansion of T cells past the onset of peak tumor burden in survivors may result from enduring cognate antigen–mediated signals, causing continued CAR T cell expansion before eventual exhaustion and contraction occurred (55). Swift contraction of CAR T cells following peak expansion indicates that target antigen density has fallen to levels no longer capable of sustaining CAR T cell expansion and that tumor elimination was achieved without immediate relapse. The biphasic pattern of DOTATOC uptake in survivors stood in stark contrast to the unrelenting increases in both T cell and tumor burdens in nonsurvivors where tumor growth was evidently surpassing the rate of killing by T cells. It would be interesting to investigate whether a similar pattern is observed in additional tumor models and in clinical studies. Finally, DOTATOC uptake values obtained in the longitudinal study enabled comparisons with uptake values derived from the SSTR2-titrated Jurkat model. This indicated that peak CAR T cell density in 8505C tumors ranged from below 1% at infusion to ~10% in survivors and to well over 10% in mice with high tumor burden.

In conclusion, we have demonstrated a clinically adaptable, quantitative imaging system capable of specifically detecting adoptively transferred CAR T cells and monitoring their target-specific expansion and contraction at the tumor site with unprecedented detail. A simple method for estimating the density of solid tumor–infiltrating T cells has also been established. We anticipate that the SSTR2 system can be easily adapted to multiple ACT models and can facilitate efforts towards increasing our understanding of the parameters behind the success and failures of ACT with particular regard to monitoring systemic toxicities and the responses to solid tumors.

Methods

Mammalian cell culture. Parental HeLa (ATCC), HEK 293 (ATCC), and 8505C (DSMZ) cells were transduced with lentivirus encoding Firefly Luciferase-F2A-GFP (Biosettia) followed by fluorescence-activated cell sorting (FACS) to purify GFP-expressing cells. HeLa-$FLuc^+GFP^+$ and HEK 293-$FLuc^+GFP^+$ cells were cultured in Advanced Dulbecco's Modified Eagle Medium containing 10% (v/v) FBS, 2 mM L-alanyl-L-glutamine dipeptide (Gibco), and 100 U/ml penicillin-streptomycin (Pen/Strep) (Gibco). 8505C-$FLuc^+GFP^+$ cells were cultured in RPMI-1640 supplemented with 10% (v/v) FBS, 2 mM L-alanyl-L-glutamine dipeptide, and 100 U/ml Pen/Strep. Human peripheral blood was obtained from healthy volunteer donors by venipuncture. Peripheral blood mononuclear cells (PBMCs) were isolated over Ficoll-Paque PLUS (GE Healthcare) and cultured in Optimizer CTS T-cell Expansion SFM (Thermo Fisher) supplemented with 5% human AB serum (Sigma-Aldrich), 2 mM L-alanyl-L-glutamine dipeptide, 100 U/ml Pen/Strep and 30 IU/ml human IL-2 (Cell Sciences). Nonadherent cells were removed after 24 hours and magnetically enriched for T cells with Dynabeads CD3/CD28 T cell expander (Thermo Fisher) at a

2:1 bead/T cell ratio. Dynabead-bound T cells were subsequently cultured in IL-2–containing media at a density of 1×10^6 to 2×10^6 cells/ml. All cells were incubated at 37°C in a 5% CO_2 humidified incubator.

Construction of ICAM-1 CAR and SSTR2 reporter genes. The CAR gene specific to ICAM-1 was derived from the scFv sequence of a murine monoclonal anti–human R6.5 antibody — itself derived from hybridoma (ATCC) (56, 57). The R6.5-specific scFv was then fused to the transmembrane and cytoplasmic domains of CD28, CD137, and CD3ζ of an independent third-generation pLenti plasmid (a gift from Carl June at the University of Pennsylvania, Philadelphia, Pennsylvania, USA) (35). A lentivirus vector (derived from the CAR vector) encoding human SSTR2 (NM_001050) was constructed by synthesizing the SSTR2-coding sequence (IDT) and inserting it into the vector using Xba1 and Sal1 sites.

Lentivirus production and transduction of T cells. Lentivirus particles were produced by transiently transfecting HEK 293 cells using calcium phosphate. Briefly, 10 μg transfer gene, 7.5 μg CMV-dR8.2 (Addgene) and 5 μg pCMV-VSVG (Addgene) were mixed and incubated with 2 M $CaCl_2$ followed by 2× Hanks' balanced salt solution (HBSS). Resulting solutions were added dropwise to 10-cm cell culture dishes seeded with 3.2×10^6 HEK 293 in 10 ml DMEM 24 hours previously. Transfection media was replaced after 6 hours. Media containing lentivirus was harvested at 48 and 72 hours after transfection, filtered through 0.45-μm filters, and concentrated by ultracentrifugation at 75,000 *g* for 2 hours at 4°C. Lentivirus was then resuspended in serum-containing media at an approximate titer of 10^8/ml and frozen at –80°C. Human T cells were transduced 24–72 hours after activation with CD3/CD28 Dynabeads either by spinfection at 1,000 *g* for 1 hour at 32°C or by overnight incubation of lentivirus in the presence of Synperonic F108 (Sigma-Aldrich) (58). T cells were also transduced a second time, 24 hours after initial transduction. The viral titer was adjusted to obtain a transduction level of approximately 50%. During and following transduction, media containing IL-2 was replaced with media containing human IL-7 (10 ng/ml) and IL-15 (5 ng/ml) (Peprotech), which was found to augment T cell persistence in vivo (59, 60). Jurkat T cells were transduced by a single incubation with lentivirus overnight in the presence of Synperonic F108.

Confirmation of SSTR2 functionality and measurement of site density. SSTR2-transduced Jurkat T cells were incubated with or without 1 μM octreotide (Sigma-Aldrich) for 30 minutes at 37 °C. Subsequent internalization of SSTR2 was measured by flow cytometry analysis of SSTR2 expression. The site density of SSTR2 expression on Jurkats was determined by incubating nontransduced and SSTR2-transduced Jurkat T cells with DOTATOC (8–250 nM) at either 37°C or 4°C for 30 minutes in PBS/0.1% BSA. After incubation, cells were washed 3 times and DOTATOC uptake was measured using a gamma counter (Packard, Cobra II Auto-Gamma). Values obtained were used for Scatchard analysis to estimate affinity and site density.

Subcutaneous Jurkat T cell xenograft. SSTR2-expressing Jurkats were spiked with increasing numbers of nontransduced Jurkats to derive distinct cultures containing defined percentages of SSTR2 expression ranging from 100%–0%. For each subcutaneous xenograft, 5×10^6 total cells were resuspended in 100 μl Matrigel Basement Membrane Matrix (Corning) and injected bilaterally into nonobese diabetic (NOD)/LtSz-*Prkdc*^{scid}*Il2rg*^{tm1Wjl}/J (NSG) mice (Jackson Laboratory). Measurements of tumor size were made using a digital caliper. Tumor volume was calculated by using the modified ellipsoid formula 0.5 × (length × width^2). Length was measured as the longer dimension. Each dimensional measurement was rounded to the nearest 0.5 mm.

Labeling of ^{68}Ga-DOTATOC. DOTATOC (1,4,7,10-tetraazacyclododecane-N^{I},N^{II},N^{III},N^{IIII}-tetraacetic acid (D)-Phe^1-thy^3-octreotide, GMP grade) was obtained as 1 mg lyophilized powder (ABX Pharmaceuticals). The DOTATOC vial content was diluted with 18 MOhm water to 2 ml (0.5 mg/ml solution) and stored at 4°C as a stock solution. ^{68}Ga was obtained by eluting an ITG ^{68}Ge/^{68}Ga generator (ITM) with 4 ml 0.05 M HCl solution. To the eluted $^{68}Ga^{3+}$, 50 μl of the DOTATOC stock solution (25 μg) was added, followed by 80 μl of a 3N NaOAc solution for buffering. The mixture was immediately placed in a Thermomixer (Eppendorf) at 95°C and incubated for 15 minutes. Following incubation, the mixture was passed through a previously activated C-18 Sep-Pak Lite (Waters) to trap the labeled peptide. The labeling vial was washed with 5 ml 18 MOhm water and the resulting wash was also passed through the C-18 Sep-Pak. Finally, the Sep-Pak was washed with an extra 5 ml of 18 MOhm water to eliminate any remaining free ^{68}Ga. The trapped ^{68}Ga-DOTATOC was then slowly eluted from the C-18 Sep-Pak using 100 μl of ethanol followed by 900 μl of saline solution for injection, providing the final product in a 10% ethanol, isotonic, injectable solution. The purity of the final product was checked by reverse-phase HPLC.

E:T assay. 2 × 10^5 HeLa-FLuc$^+$GFP$^+$, 8505c-FLuc$^+$GFP$^+$, or HEK 293-FLuc$^+$GFP$^+$ cells were cocultured with either nontransduced or CAR-expressing T cells (SSTR2-R6.5 or R6.5) at varying E:T ratios as indicated. Cocultures were carried out in T cell media containing 150 μg/ml D-luciferin (Gold Biotechnology) with no cytokine supplementation. Luminescence was measured using a plate reader (TECAN infinite M1000 PRO) with readings in each E:T condition normalized to the nontransduced T cell/target coculture controls.

8505C mouse model, measurement of ex vivo organs and whole-body tumor growth. 8505c-FLuc$^+$GFP$^+$ cells (1 × 10^6) were injected into NSG mice via tail vein. Primary human T cells (2 × 10^6 to 3 × 10^6) were injected via tail vein 7–15 days after tumor cell injection. Luminescence imaging of tumor xenografts in live mice was performed using a whole-body optical imager (In-Vivo Extreme 4MP, Bruker). Mice were first anesthetized with 3% isoflurane at 2 l/min O_2 and subsequent to this, maintained at 2% isoflurane at 2 l/min O_2. Growth or reduction in tumor burden was estimated by integration of luminescence over the lungs or the entire mouse body. Ex vivo fluorescence imaging of mouse liver, lungs, spleen, and resected tumors was performed using a whole-body optical imager (In-Vivo F Pro, Bruker).

PET/CT imaging. Registered CT images were acquired using a micro-PET/CT scanner (Inveon, Siemens) 1–2 hours after DOTATOC injection. Projection data were acquired in a cone-beam geometry with approximately 1-second steps at 1° angular increments. At least 10 × 10^6 coincidence events were acquired for PET per study using a 250- to 750-keV energy window and a 6-nanosecond timing window. A reference was included using a tube containing 100 μl of 10 %ID/cm^3 for quantification of DOTATOC uptake in vivo. To compute DOTATOC uptake by Jurkat tumors, the ellipsoidal ROIs (AMIDE software; http://amide.sourceforge.net/index.html) were placed to enclose subcutaneous tumors that closely match overall tumor size and shape. For systemic 8505C tumor models, ellipsoids were drawn separately on the left and right sides of lungs to enclose all 5 lobes of mouse lungs. The %ID/cm^3 values, computed relative to the counts in a reference tube, can be approximated to a standard uptake value (SUV) (61) by dividing %ID/cm^3 by 4, assuming an injection efficiency of 100% and 25 g body weight. Visualization and analyses of PET/CT images were performed using AMIDE.

Flow cytometry. Jurkat tumor xenografts or mouse organs (lungs and liver) were harvested from mice following completion of PET/CT imaging. Tissues were diced and flushed through an 80-μm cell strainer to yield single-cell suspensions. Red blood cells were lysed by incubating the cell suspension with 1× Ammonium-Chloride-Potassium lysing buffer (Thermo Fisher), followed by washing and resuspension in 1× HBSS containing 2% normal goat serum. Prior to staining, cells were blocked with mouse IgG (Sigma-Aldrich, 15381) at 2 μg/ml for 10 minutes. This was followed by live staining with 1 μg/ml propidium iodide (PI, Invitrogen, P3566) in combination with 2 μg/ml murine anti–human CD3-Alexa Fluor 647 (Biolegend, 300322) or 2 μg/ml PE-conjugated murine anti–human SSTR2 (R&D Systems, FAB4224P). Flow cytometry gates were first determined by live-cell gating (PI negative) and subsequently by staining of respective antibodies. ICAM-1 expression on tumor cell lines was determined using a murine anti–human R6.5 monoclonal antibody (10 μg/ml) derived from hybridoma (ATCC) (57). R6.5-CAR expression on T cells was detected using FITC-conjugated goat anti–mouse F(ab′)2 secondary antibody (Thermo Fisher, 31543).

Histology. Jurkat tumor xenografts were harvested, fixed in 4% paraformaldehyde in PBS, embedded in paraffin, and were cut to produce 5-μm sections (Microtome, Leica). Paraffin-embedded sections were stained with hematoxylin and eosin (H&E) or hematoxylin only for CD3 immunostaining (performed by HistoWiz, Inc.). After euthanasia, mouse lungs were perfused via the trachea with 4% paraformaldehyde, and each of 5 lobes was separated after fixation and embedded in paraffin. Liver tissue was harvested and processed identically for histology. Histological analysis was performed by an experienced pathologist.

Statistics. One-way ANOVA and unpaired, 2-tailed Student's *t* test were performed using Prism 7 (GraphPad) on data indicated. A *P* value less than 0.05 was considered significant.

Study approval. The protocol for blood draw from healthy volunteers is approved by the Institutional Review Board of Weill Cornell Medicine (permit number: 1302013613). All animal experiments were performed in strict accordance with the recommendations contained within the National Institute of Health's Guide for the Care and Use of Laboratory Animals and animal handling protocols were approved by the Institutional Laboratory Animal Use and Care Committee of Weill Cornell Medicine (permit number: 2012-0063).

Author contributions

MMJ conceived, designed, and oversaw the study. YV, ES, and MZ are the primary authors of the manuscript and performed the majority of experiments. Additional experiments were performed by IMM, Spencer Park, Susan Park, KK, TS, and MMJ. AA synthesized ^{68}Ga-DOTATOC. DK oversaw PET/CT imaging. YK is a pathologist, and reviewed pathological specimens. BL, RT, and JB contributed reagents and expertise. MMJ, ES, YV, and Susan Park wrote the manuscript. All authors have reviewed and approved the manuscript.

Acknowledgments

We are grateful to Maureen Moore for technical assistance. Funding: NIH grants R01CA178007, P50 CA172012, and R21AI107451. This research was partially supported by the Basic Science Research Program (to K.W. Kwon) through the National Research Foundation of Korea (NRF) funded by the Ministry of Education (357-2011-1-D00292).

Address correspondence to: Moonsoo M. Jin, Department of Radiology, Weill Cornell Medical College, BB-1514, 413 E. 69th St., New York, New York 10065, USA. Phone: 646.962.6115; E-mail: moj2005@med.cornell.edu.

1. Rosenberg SA, Restifo NP. Adoptive cell transfer as personalized immunotherapy for human cancer. *Science*. 2015;348(6230):62–68.
2. Porter DL, Levine BL, Kalos M, Bagg A, June CH. Chimeric antigen receptor-modified T cells in chronic lymphoid leukemia. *N Engl J Med*. 2011;365(8):725–733.
3. Brentjens R, Yeh R, Bernal Y, Riviere I, Sadelain M. Treatment of chronic lymphocytic leukemia with genetically targeted autologous T cells: case report of an unforeseen adverse event in a phase I clinical trial. *Mol Ther*. 2010;18(4):666–668.
4. Teachey DT, et al. Identification of predictive biomarkers for cytokine release syndrome after chimeric antigen receptor T-cell therapy for acute lymphoblastic leukemia. *Cancer Discov*. 2016;6(6):664–679.
5. McCracken MN, Vatakis DN, Dixit D, McLaughlin J, Zack JA, Witte ON. Noninvasive detection of tumor-infiltrating T cells by PET reporter imaging. *J Clin Invest*. 2015;125(5):1815–1826.
6. Pittet MJ, et al. In vivo imaging of T cell delivery to tumors after adoptive transfer therapy. *Proc Natl Acad Sci U S A*. 2007;104(30):12457–12461.
7. de Jong M, Essers J, van Weerden WM. Imaging preclinical tumour models: improving translational power. *Nat Rev Cancer*. 2014;14(7):481–493.
8. Kircher MF, Gambhir SS, Grimm J. Noninvasive cell-tracking methods. *Nat Rev Clin Oncol*. 2011;8(11):677–688.
9. Ahrens ET, Bulte JW. Tracking immune cells in vivo using magnetic resonance imaging. *Nat Rev Immunol*. 2013;13(10):755–763.
10. Liu Z, Li Z. Molecular imaging in tracking tumor-specific cytotoxic T lymphocytes (CTLs). *Theranostics*. 2014;4(10):990–1001.
11. Herschman HR. Micro-PET imaging and small animal models of disease. *Curr Opin Immunol*. 2003;15(4):378–384.
12. Boissonnas A, Fetler L, Zeelenberg IS, Hugues S, Amigorena S. In vivo imaging of cytotoxic T cell infiltration and elimination of a solid tumor. *J Exp Med*. 2007;204(2):345–356.
13. Yaghoubi SS, et al. Noninvasive detection of therapeutic cytolytic T cells with ^{18}F-FHBG PET in a patient with glioma. *Nat Clin Pract Oncol*. 2009;6(1):53–58.
14. Yaghoubi S, et al. Human pharmacokinetic and dosimetry studies of [(18)F]FHBG: a reporter probe for imaging herpes simplex virus type-1 thymidine kinase reporter gene expression. *J Nucl Med*. 2001;42(8):1225–1234.
15. Peñuelas I, et al. Positron emission tomography imaging of adenoviral-mediated transgene expression in liver cancer patients. *Gastroenterology*. 2005;128(7):1787–1795.
16. Su H, Chang DS, Gambhir SS, Braun J. Monitoring the antitumor response of naive and memory CD8 T cells in RAG1$^{-/-}$ mice by positron-emission tomography. *J Immunol*. 2006;176(7):4459–4467.
17. Barton KN, et al. Phase I study of noninvasive imaging of adenovirus-mediated gene expression in the human prostate. *Mol Ther*. 2008;16(10):1761–1769.
18. Castanares MA, et al. Evaluation of prostate-specific membrane antigen as an imaging reporter. *J Nucl Med*. 2014;55(5):805–811.
19. Zhang H, et al. Imaging expression of the human somatostatin receptor subtype-2 reporter gene with ^{68}Ga-DOTATOC. *J Nucl Med*. 2011;52(1):123–131.
20. Moroz MA, et al. Comparative analysis of T cell imaging with human nuclear reporter genes. *J Nucl Med*. 2015;56(7):1055–1060.
21. Griessinger CM, et al. In vivo tracking of Th1 cells by PET reveals quantitative and temporal distribution and specific homing in lymphatic tissue. *J Nucl Med*. 2014;55(2):301–307.
22. Dobrenkov K, et al. Monitoring the efficacy of adoptively transferred prostate cancer-targeted human T lymphocytes with PET and bioluminescence imaging. *J Nucl Med*. 2008;49(7):1162–1170.
23. Yamada Y, Post SR, Wang K, Tager HS, Bell GI, Seino S. Cloning and functional characterization of a family of human and mouse somatostatin receptors expressed in brain, gastrointestinal tract, and kidney. *Proc Natl Acad Sci U S A*. 1992;89(1):251–255.
24. Garkavij M, et al. ^{177}Lu-[DOTA0,Tyr3] octreotate therapy in patients with disseminated neuroendocrine tumors: Analysis of

dosimetry with impact on future therapeutic strategy. *Cancer*. 2010;116(4 Suppl):1084–1092.
25. Kratochwil C, et al. ^{213}Bi-DOTATOC receptor-targeted alpha-radionuclide therapy induces remission in neuroendocrine tumours refractory to beta radiation: a first-in-human experience. *Eur J Nucl Med Mol Imaging*. 2014;41(11):2106–2119.
26. Wulfert S, et al. Multimodal imaging for early functional response assessment of (90)Y-/ (177)Lu-DOTATOC peptide receptor targeted radiotherapy with DW-MRI and (68)Ga-DOTATOC-PET/CT. *Mol Imaging Biol*. 2014;16(4):586–594.
27. Koyama S, Ebihara T, Fukao K. Expression of intercellular adhesion molecule 1 (ICAM-1) during the development of invasion and/or metastasis of gastric carcinoma. *J Cancer Res Clin Oncol*. 1992;118(8):609–614.
28. Tempia-Caliera AA, et al. Adhesion molecules in human pancreatic cancer. *J Surg Oncol*. 2002;79(2):93–100.
29. Shimoyama S, Gansauge F, Gansauge S, Widmaier U, Oohara T, Beger HG. Overexpression of intercellular adhesion molecule-1 (ICAM-1) in pancreatic adenocarcinoma in comparison with normal pancreas. *Pancreas*. 1997;14(2):181–186.
30. Buitrago D, et al. Intercellular adhesion molecule-1 (ICAM-1) is upregulated in aggressive papillary thyroid carcinoma. *Ann Surg Oncol*. 2012;19(3):973–980.
31. Guo P, et al. ICAM-1 as a molecular target for triple negative breast cancer. *Proc Natl Acad Sci U S A*. 2014;111(41):14710–14715.
32. Chen X, et al. Inflamed leukocyte-mimetic nanoparticles for molecular imaging of inflammation. *Biomaterials*. 2011;32(30):7651–7661.
33. Rivera M, Ghossein RA, Schoder H, Gomez D, Larson SM, Tuttle RM. Histopathologic characterization of radioactive iodine-refractory fluorodeoxyglucose-positron emission tomography-positive thyroid carcinoma. *Cancer*. 2008;113(1):48–56.
34. Higgins MJ, Forastiere A, Marur S. New directions in the systemic treatment of metastatic thyroid cancer. *Oncology (Williston Park, NY)*. 2009;23(9):768–775.
35. Carpenito C, et al. Control of large, established tumor xenografts with genetically retargeted human T cells containing CD28 and CD137 domains. *Proc Natl Acad Sci USA*. 2009;106(9):3360–3365.
36. Cescato R, et al. Internalization of sst2, sst3, and sst5 receptors: effects of somatostatin agonists and antagonists. *J Nucl Med*. 2006;47(3):502–511.
37. Zou KH, O'Malley AJ, Mauri L. Receiver-operating characteristic analysis for evaluating diagnostic tests and predictive models. *Circulation*. 2007;115(5):654–657.
38. Cosimi AB, et al. In vivo effects of monoclonal antibody to ICAM-1 (CD54) in nonhuman primates with renal allografts. *J Immunol*. 1990;144(12):4604–4612.
39. Kim JH, et al. High cleavage efficiency of a 2A peptide derived from porcine teschovirus-1 in human cell lines, zebrafish and mice. *PLoS One*. 2011;6(4):e18556.
40. Zhang L, Gaskins K, Yu Z, Xiong Y, Merino MJ, Kebebew E. An in vivo mouse model of metastatic human thyroid cancer. *Thyroid*. 2014;24(4):695–704.
41. Turtle CJ, et al. CD19 CAR-T cells of defined $CD4^+$:$CD8^+$ composition in adult B cell ALL patients. *J Clin Invest*. 2016;126(6):2123–2138.
42. Yaghoubi SS, Campbell DO, Radu CG, Czernin J. Positron emission tomography reporter genes and reporter probes: gene and cell therapy applications. *Theranostics*. 2012;2(4):374–391.
43. Kratochwil C, et al. SUV of [^{68}Ga]DOTATOC-PET/CT predicts response probability of PRRT in neuroendocrine tumors. *Mol Imaging Biol*. 2015;17(3):313–318.
44. Buchmann I, et al. Comparison of ^{68}Ga-DOTATOC PET and ^{111}In-DTPAOC (Octreoscan) SPECT in patients with neuroendocrine tumours. *Eur J Nucl Med Mol Imaging*. 2007;34(10):1617–1626.
45. Forrer F, Uusijärvi H, Storch D, Maecke HR, Mueller-Brand J. Treatment with ^{177}Lu-DOTATOC of patients with relapse of neuroendocrine tumors after treatment with ^{90}Y-DOTATOC. *J Nucl Med*. 2005;46(8):1310–1316.
46. Velikyan I, et al. Quantitative and qualitative intrapatient comparison of ^{68}Ga-DOTATOC and ^{68}Ga-DOTATATE: net uptake rate for accurate quantification. *J Nucl Med*. 2014;55(2):204–210.
47. Yaghoubi SS, Gambhir SS. PET imaging of herpes simplex virus type 1 thymidine kinase (HSV1-tk) or mutant HSV1-sr39tk reporter gene expression in mice and humans using [^{18}F]FHBG. *Nat Protoc*. 2006;1(6):3069–3075.
48. Berger C, Flowers ME, Warren EH, Riddell SR. Analysis of transgene-specific immune responses that limit the in vivo persistence of adoptively transferred HSV-TK-modified donor T cells after allogeneic hematopoietic cell transplantation. *Blood*. 2006;107(6):2294–2302.
49. Riddell SR, et al. T-cell mediated rejection of gene-modified HIV-specific cytotoxic T lymphocytes in HIV-infected patients. *Nat Med*. 1996;2(2):216–223.
50. Doubrovin MM, Doubrovina ES, Zanzonico P, Sadelain M, Larson SM, O'Reilly RJ. In vivo imaging and quantitation of adoptively transferred human antigen-specific T cells transduced to express a human norepinephrine transporter gene. *Cancer Res*. 2007;67(24):11959–11969.
51. Hinrichs CS, et al. Adoptively transferred effector cells derived from naive rather than central memory $CD8^+$ T cells mediate superior antitumor immunity. *Proc Natl Acad Sci USA*. 2009;106(41):17469–17474.
52. Klebanoff CA, et al. Central memory self/tumor-reactive $CD8^+$ T cells confer superior antitumor immunity compared with effector memory T cells. *Proc Natl Acad Sci USA*. 2005;102(27):9571–9576.
53. Vatakis DN, et al. Antitumor activity from antigen-specific CD8 T cells generated in vivo from genetically engineered human hematopoietic stem cells. *Proc Natl Acad Sci USA*. 2011;108(51):E1408–E1416.
54. Grupp SA, et al. Chimeric antigen receptor-modified T cells for acute lymphoid leukemia. *N Engl J Med*. 2013;368(16):1509–1518.
55. van Stipdonk MJ, Lemmens EE, Schoenberger SP. Naïve CTLs require a single brief period of antigenic stimulation for clonal expansion and differentiation. *Nat Immunol*. 2001;2(5):423–429.
56. Smith CW, et al. Recognition of an endothelial determinant for CD 18-dependent human neutrophil adherence and transendothelial migration. *J Clin Invest*. 1988;82(5):1746–1756.
57. Leelawattanachai J, Kwon KW, Michael P, Ting R, Kim JY, Jin MM. Side-by-side comparison of commonly used biomolecules that differ in size and affinity on tumor uptake and internalization. *PLoS One*. 2015;10(4):e0124440.
58. Höfig I, Atkinson MJ, Mall S, Krackhardt AM, Thirion C, Anastasov N. Poloxamer synperonic F108 improves cellular trans-

duction with lentiviral vectors. *J Gene Med*. 2012;14(8):549–560.
59. Gargett T, Brown MP. Different cytokine and stimulation conditions influence the expansion and immune phenotype of third-generation chimeric antigen receptor T cells specific for tumor antigen GD2. *Cytotherapy*. 2015;17(4):487–495.
60. Xu Y, et al. Closely related T-memory stem cells correlate with in vivo expansion of CAR.CD19-T cells and are preserved by IL-7 and IL-15. *Blood*. 2014;123(24):3750–3759.
61. Kinahan PE, Fletcher JW. Positron emission tomography-computed tomography standardized uptake values in clinical practice and assessing response to therapy. *Semin Ultrasound CT MR*. 2010;31(6):496–505.